analytical chemistry

Article

Cite This: Anal. Chem. 2020, 92, 1355−1362

pubs.acs.org/ac

Three-Dimensional Composition Analysis of SnAg Solder Bumps Using Ultraviolet Femtosecond Laser Ablation Ionization Mass Spectrometry

A. Cedeño López,*[,†] V. Grimaudo,[‡] A. Riedo,[§] M. Tulej,[‡] R. Wiesendanger,[‡] R. Lukmanov,[‡] P. Moreno-García,[†] E. Lörtscher,[∥] P. Wurz,[‡] and P. Broekmann[†]

[†]Department of Chemistry and Biochemistry, Interfacial Electrochemistry Group, University of Bern, Freiestrasse 3, 3012 Bern, Switzerland

[‡]Physics Institute, Space Research and Planetary Sciences, University of Bern, Sidlerstrasse 5, 3012 Bern, Switzerland

[§]Laboratory for Astrophysics, Leiden Observatory, Leiden University, Niels Bohrweg 2, 2333 CA Leiden, The Netherlands

[∥]IBM Research Zurich, Säumerstrasse 4, 8803 Rüschlikon, Switzerland

Supporting Information

ABSTRACT: The application of a novel UV fs Laser Ablation Ionization Mass Spectrometry approach for chemical depth profiling of low-melting point, high surface roughness SnAg solder bump features is presented. The obtained submicrometer resolved three-dimensional compositional data reveal unprecedented information on the distribution of individual elements inside the solder bump matrix. Moreover, the determination of matrix-matched relative sensitivity coefficients allows the first report on quantitative assessment of the SnAg alloy composition. These results significantly contribute to an in-depth understanding of the SnAg plating process. This experimental procedure may find application in future additive performance screening.

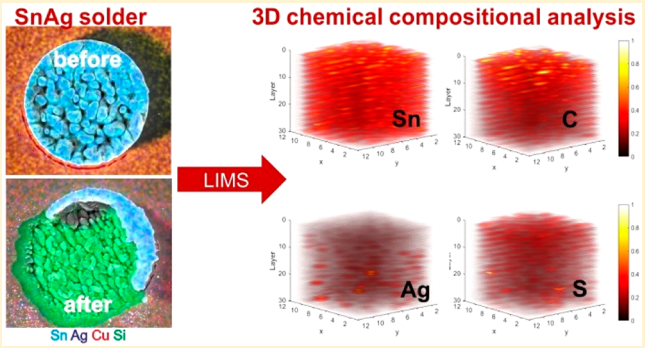

Solder materials have increasingly gained importance in microelectronics not only in second level packaging, i.e., on the level of printed circuit board assembly, but also in first level packaging, e.g., flip-chip assembly as illustrated in Figure 1 panel a).[1] In these applications, various types of solder bumps with distinct dimensions are used for the sophisticated interconnection of three-dimensional integrated circuits (3D-ICs).[1a] The schematics of the buildup of a typical solder bump are shown in Figure 1 panel b). The technologically most relevant alloy material of today's solder bumping applications on the 300 mm wafer level is electrodeposited eutectic SnAg.[1b] However, fabrication of the SnAg alloy by electrochemical deposition is a challenging task due to the large difference in standard reduction potentials of the Sn^{2+} and Ag^{+} ions ($\Delta E^0 \approx 0.94$ V). To circumvent this issue, complexing and chelating agents that act selectively on the nobler Ag^{+} ions, thus slowing down their deposition rate to be compatible with the one of Sn^{2+}, and facilitating codeposition of the two metals, are typically added to the SnAg plating baths[2] as a crucial prerequisite to achieve the desired alloy composition.[3] Another complementary function of such complexing and chelating agents is the stabilization of the Ag^{+} ions in the Sn-containing electrolyte that prevents their reduction to metallic Ag and the concomitant oxidation of Sn^{2+} to Sn^{4+}, thus avoiding the precipitation of Ag colloids. Furthermore, high quality electrodeposition requires the use of surfactants and antioxidants in the plating bath. However, the high organic load of the bath implies the risk of additive incorporation into the alloy matrix. This is a highly undesirable effect, as the performance and lifetime of solder joints formed from the electrodeposit suffer strongly from compositional inhomogeneities, and nonmetallic inclusions. To which extent additive incorporation occurs in SnAg plating is not known to date. For additive screening purposes, laterally expanded SnAg films are commonly prepared, as their fabrication is simpler and less expensive than the one of SnAg solder bumps. Scanning Electron Microscopy (SEM) images of the two generally different concepts of SnAg films and bumps are shown in Figure S1 in the Supporting Information (SI). Due to pronounced differences in the mass transport and current density distribution conditions between these systems in the electrolytic process, it cannot intrinsically be assumed that results obtained on the simplified planar model substrates are transferable to the spatially confined solder bumps used in actual microelectronic applications. Hence, high spatial resolution depth profiling of SnAg solder bumps is a prerequisite to obtain an understanding

Received: October 4, 2019
Accepted: December 6, 2019
Published: December 20, 2019

DOI: 10.1021/acs.analchem.9b04530
Anal. Chem. 2020, 92, 1355−1362

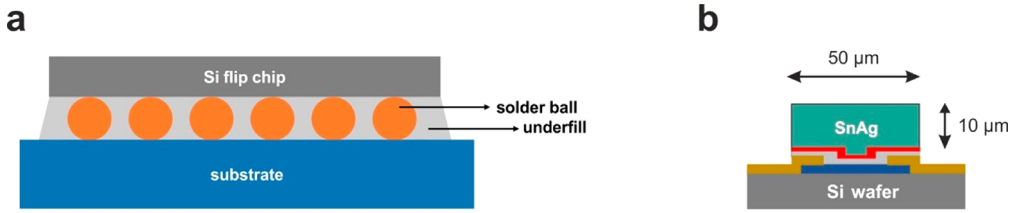

Figure 1. Schematic representation of the flip chip packaging concept (panel a) and the buildup of a typical solder bump feature as investigated in this study (panel b).[16]

Table 1. Composition of Chemistries A and B

chemical name	mL Chemistry A	mL Chemistry B
methane sulfonic acid	25	25
tin methane sulfonate, stabilized	6.45	6.45
complexed silver methane sulfonate solution (Ag^+:complexing agent = 1:2n)	0.25−7.5	1.25
surfactant	0.23	0.23

of their additive-assisted plating process that may bring forward significant optimization potential in industrial plating formulations. Among the various analytical techniques capable of providing high resolution chemical composition information, Laser-Induced Breakdown Spectroscopy (LIBS) studies have proven this method's high potential in surface analysis. However, lateral and depth resolution as well as detection sensitivity were reported to be lower than that for Laser Ablation Time-Of-Flight Mass Spectrometry (LA-TOF-MS).[4] Laser Ablation Inductively Coupled Plasma Mass Spectrometry (LA-ICP-MS) is able to yield lateral resolution in the micrometer and depth resolution in the submicrometer range and outperforms Auger electron spectroscopy (AES) and Secondary Ion Mass Spectrometry (SIMS) regarding matrix effects and limitations in bulk analysis capabilities.[5] LA-ICP-MS might be a higher spatial resolution alternative for well-established analysis techniques like Glow-Discharge Optical Emission Spectroscopy (GD-OES).[6] However, the quantitative detection of O and N is only possible with LA-ICP-MS if the ICP is hermetically sealed against air, which most often does not apply.[7] Also the quantitative detection of C is a challenging task for LA-ICP-MS, as the ionization efficiency of C in the ICP is only ∼1−5%.[8] Tandem LA-ICP-MS and LIBS instrumentation may be applied to overcome this limitation. Laser Ablation Ionization Mass Spectrometry (LIMS) has been demonstrated to perform comparatively well concerning lateral and depth resolution as LA-ICP-MS, even on technically demanding samples like low melting point, high surface roughness, μm-sized as-deposited SnAg solder bumps.[9] Furthermore, LIMS provides the possibility to quantify O and N due to the high vacuum working conditions, and the ionization efficiency of C does not constrain LIMS analysis. Therefore, LIMS is ideally suited for the investigation of organic additive embedment into metal electrodeposits.

In this study, we present the application of a recently developed UV fs LIMS depth profiling approach for SnAg solder bump features at optimized experimental conditions.[9f] The performance of this experimental approach is compared to commonly applied analytical techniques, namely Energy Dispersive X-ray Spectroscopy (EDX) and Inductively Coupled Plasma Mass Spectrometry (ICP-MS). The analysis of a matrix-matched, certified reference sample further allows for the determination of relative sensitivity coefficients (RSCs) for Sn and Ag. On the basis of these calibration factors we can, for the first time, quantitatively assess the concentrations and the spatial distribution of the metallic constituents in the SnAg solder bumps by means of LIMS measurements. A multiposition binning approach for a layer-by-layer removal and analysis of sample material was applied.[9f] With the help of a dedicated software tool, the 2D-binned data were for the first time converted into three-dimensional representations, which allow for tracing the distribution of different elements in a solder alloy bump in unprecedented detail.

Our current study particularly focuses on the surface and near-surface bulk regions of the as-deposited SnAg bumps. This is important because the roughness of the samples is typically highest on the surface due to the characteristics of the electroplating process, which renders them especially prone to contamination from the plating bath as organic molecules may adhere onto irregularities or be entrapped in cavities. This makes the surface and near-surface bulk region of SnAg solder bumps most challenging with regard to spatially resolved chemical analysis. We demonstrate herein that our analysis concept is robust enough to tackle these challenges and to yield three-dimensional chemical compositional data even on these sections of the SnAg bump.

EXPERIMENTAL SECTION

Electrochemical Deposition (ECD) of SnAg Films and Bumps. SnAg films and bumps for EDX and ICP-MS analysis as well as SnAg bumps for SEM/Atomic Force Microscopy (AFM) and LIMS analysis were prepared galvanostatically on blanket, 100 nm Cu-seeded Si wafer coupons (Hionix, U.S.A.) in case of the films and on patterned 100 nm Cu-seeded Si wafer coupons (IMEC, Belgium) in case of the bumps. SEM images of the different substrates are shown in Figure S1 in the SI. A potentiostat/galvanostat PGSTAT128N (Metrohm Autolab, Switzerland) was used in all cases. The wafer coupons, individually fixed onto a rotating disk electrode (RDE), served as the cathode, a Pt wire as the anode, and an Ag/AgCl (3 M KCl) double junction electrode (Metrohm, Switzerland) was used as the reference electrode. The plating bath composition (BASF SE, Ludwigshafen, Germany) and the applied plating parameters are given in Tables 1 and 2, respectively. Plating additive quantities are stated in mL (total bath volume: 250 mL), as their molecular weight is undisclosed information. For the SnAg films and bumps for EDX and ICP-MS analysis, Chemistry A and plating parameter set 1 were used. The SnAg

DOI: 10.1021/acs.analchem.9b04530
Anal. Chem. 2020, 92, 1355−1362

Table 2. Plating Parameter Sets 1 and 2

plating parameter set	layer thickness (μm)	current density (mA/cm^2)	rotational speed (rpm)
1	0.25−10	−150	800
2	10	−150	800

bumps for the SEM/AFM-based investigation were obtained with Chemistry B and plating parameter set 1. The SnAg bumps for LIMS analysis were obtained with Chemistry B and plating parameter set 2.

LIMS Measurements. The basic operation mode and the performance of the LIMS instrument used in this study have been described in detail in previous publications.[10] The ionization source, a fs-laser beam (pulse width of ∼190 fs), has a fundamental wavelength of 775 nm and a Gaussian beam profile. Newly implemented harmonic generators (Storc, Clark-MXR Inc., U.S.A.) yield radiation at the second (387 nm) and third (258 nm) harmonic of the fundamental laser beam, i.e., the experimental setup is operated as a UV-fs laser system. All of the LIMS experiments in this study were performed at a laser wavelength of 258 nm. An optical microscope system inside the vacuum chamber enables precise sample positioning.[11] This is crucial for the application of our novel 2D raster approach introduced recently.[9f] In short, this approach is based on a software tool that uses the bump center coordinates to calculate a circular raster pattern of the laser shots with a defined shot pitch distance, which ideally suits the bump geometry and allows to ablate top-down the entire feature layer-by-layer if the overlap between the shot positions is sufficiently high. Analyses of a matrix-matched, certified reference sample (BCS-CRM No. 347, BAS Ltd., U.K.) were carried out with 15 000 laser shots each at six different pulse energies between 0.15 and 0.51 μJ to determine RSC values for Sn and Ag. Depth profiling experiments with the 2D raster approach were carried out at 0.33 μJ and with a laser shot pitch distance of 4 μm resulting in layers with 121 binned shot positions each. Thirty such layers were acquired to assess the chemical composition of the surface and early bulk region of the bump feature.

PDMS Casting. To obtain a negative imprint of the bumps after depth profiling, a previously established PDMS (polydimethylsiloxan) imprinting protocol for LIMS craters was applied to the samples.[9d] For the SEM inspection of the PDMS imprints a thin Au layer was sputtered onto the mold to obtain a conductive surface.

SEM and EDX Measurements. SEM micrographs and composition maps were recorded with a Zeiss Gemini SEM (Zeiss, Germany) at an accelerating voltage of 10 kV and a working distance of 8.5 mm. EDX spectra were recorded with a Hitachi S-3000N SEM (Hitachi, Japan) applying an accelerating voltage of 25 keV at a working distance of 10 mm. EDX data were averaged over 2 independent samples with 3 analysis spots on each sample.

ICP-MS. For the elemental analysis by means of ICP-MS, SnAg alloy samples were dissolved in 3% nitric acid and the Sn and Ag content quantified with a 700× Agilent system.

AFM Measurements. AFM images of electrodeposited bumps were recorded with a FlexAFM V5+, 100 μm scan head (Nanosurf AG, Switzerland) mounted onto a FlexAFM 5 Sample Stage Pillar Kit 204 (Nanosurf AG, Switzerland) in tapping mode using Tap150Al-G cantilevers (Innovative Solutions Bulgaria Ltd., Bulgaria). Images were recorded with a frame size of 75 × 75 μm^2 at 256 points/line and 6s/line.

RESULTS

The overall surface roughness of the electrodeposited SnAg alloy material scales with the layer thickness (deposition time), as can be seen in the SEM and AFM studies in Figure S2, panels a and b, respectively, in the SI. This is because of the prevalence of dominant mass transport limitations in advanced stages of the electrodeposition process. Therefore, fewer nucleation centers are available as the layer thickness increases upon deposition and the formed crystallites hence grow larger. The resulting high degree of surface roughness may lead to the entrapment or chemisorption of contaminants inside or on top of the electrodeposit during plating.[12] Therefore, the amount of embedded organic impurities originating from the plating bath is expected to be highest on the very surface and in the early bulk region of the as-deposited alloy, an effect that becomes increasingly important in an advanced stage of the plating process yielding extremely roughened surface morphologies (Figure S2).

Figure 2 panel a illustrates the 2D binning depth profiling approach toward spatially resolved chemical depth profiling analysis of SnAg solder bumps.[9f] In this approach, a software-calculated raster of 121 individual laser spot positions with a center to center distance of 4 μm was applied to the as-deposited solder bump. This small center distance with a strong degree of overlap between the individual laser spots was found to yield optimum depth profiling results in previous proof-of-concept studies. Figure 2, panel b, displays an EDX map illustrating that the bump can entirely be ablated down to the underlying Si substrate when a sufficient number of iterations of the 2D raster array at elevated laser pulse energies (here: 0.51 μJ, 100 repetitions) is applied. In fact, for the conditions used to obtain the results shown in panel b, it is even feasible to drill into the Si

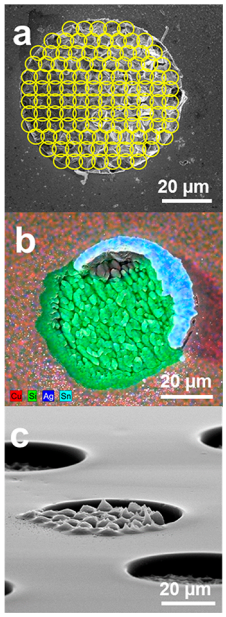

Figure 2. (a) Depiction of the shot pattern applied in the 2D binning approach for the measurement of the SnAg bump (121 positions per layer, crater pitch 4 μm); (b) EDX mapping of the resulting surface morphology after the laser ablation process (100 layer iterations at an elevated laser pulse energy of 0.51 μJ); and (c) SEM image of the PDMS replica showing a negative imprint of the surface morphology depicted in b.

DOI: 10.1021/acs.analchem.9b04530
Anal. Chem. 2020, 92, 1355−1362

substrate. This is exemplarily demonstrated in Figure 2 panel c, where an SEM image of the PDMS replica of the resulting ablation craters from the 2D raster array campaign in panel b is shown. Note that the central part of panel c displays the negative 3D imprint, i.e., the bottom-up view, of the crater shown in panel b. It is obvious that the plane of the ablated craters comes to lie higher in the imprint than the base plane from the Cu-seeded Si substrate of the original wafer coupon. As can be seen, the 2D layer binning approach allows for avoiding the formation of the cone-shaped crater profiles typically seen in 1D laser ablation depth profiling. Instead, the entire surface plane of the bump is ablated layer by layer. It has to be noted that in the experiment shown in Figure 2 a small fraction of the SnAg bump material remained on the wafer coupon and was not ablated. To avoid undesired signal contributions from this material which could deteriorate the spatial resolution of the obtained depth profile, a spatially resolved analysis should be restricted to the inner part of the bump, where all material was homogeneously removed. This is possible as mass spectra for every single laser shot were recorded for the entire measurement campaign.

A reliable quantification of the element abundances of the LIMS depth profiling results requires the determination of relative sensitivity coefficients (RSCs) for the individual elements. The RSC describes how accurate the detection of the LIMS instrument is with respect to the quantification of a given element and can be used for the accurate quantification of the experimentally measured data. RSCs are calculated via:

$$\mathrm{RSC}^X = \frac{A^X/A^{\mathrm{tot}}}{P^X}$$

where X is denoting a particular element. A stands for the area of the peak in the recorded spectrum scaled and converted to the corresponding amount of the element. A^X is the area of element X in the particular measurement. A^{tot} gives the sum of the areas of all elements in a measurement. The ratio of A^X and A^{tot} yields the experimentally measured abundance of element X. P^X denotes the certified abundance of element X in the reference material.[13] For their determination, a certified reference material is required. In our study, we use a matrix-matched certified reference sample for RSC determination of Sn and Ag (BCS-CRM No. 347, BAS Ltd., U.K.). This sample has an Sn content of 62.6 ± 0.2 wt % and an Ag content of 0.099 ± 0.007 wt % and closely resembles the studied SnAg system. Figure 3 shows the results of measurements averaged over 15 000 laser shots each for six different laser pulse energies between 0.15 and 0.51 μJ. The respective measurement campaigns are labeled "C1 to C6" in Figure 3. The red dotted line indicates the value for the Ag/Sn wt % ratio as certified in the reference sample (1.58×10^{-3}), which is hence referred to as the "expected ratio". Three distinct regimes are observed in Figure 3 for the measured Ag/Sn ratios (black squares) and the resulting RSC values (blue crosses). First, for the lower pulse energy campaigns C1 and C2, the measured Ag/Sn ratio is larger than the expected one. This can be rationalized by the fact that the signal-to-noise ratio is low for these pulse energies, leading to a noise-related overestimation of the Ag signal. Correspondingly, the RSC or scaling factor for the Ag/Sn ratio is smaller than 1 in these two cases. Second, for the medium pulse energy campaigns C3 to C5, the measured Ag/Sn ratio is satisfactorily close to the expected ratio. These are in fact nearly optimal ablation conditions, and the respective RSC values are close to 1 (C3:1.03; C4:0.89; C5:1.12). Third, for the elevated pulse energy campaign C6, the measured Ag/Sn ratio is lower than the expected one. This is most likely caused by space

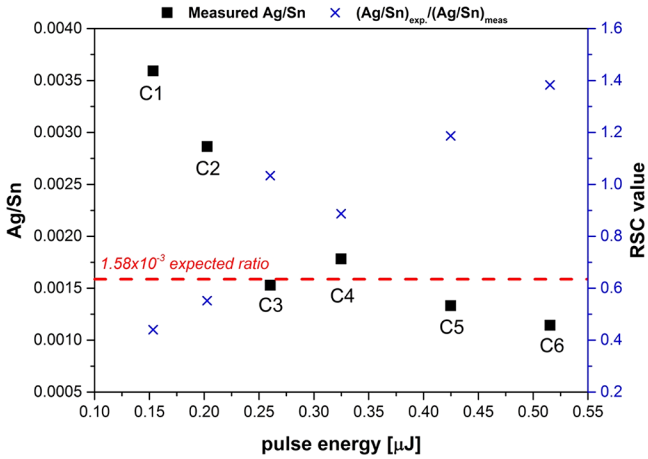

Figure 3. Determination of RSC values for the Ag/Sn ratio on a certified reference material (BCS-CRM No. 347, BAS Ltd., U.K.) for different laser pulse energies ("C1 to C6"). The measured data points (black ■) are averaged over 15 000 laser shot mass spectra each. The red dotted line represents the ratio between Ag and Sn as certified in the reference sample. The RSC values are indicated by the blue crosses. The Ag/Sn ratios displayed on the left y-axis were determined as follows: [accumulated signal for Ag (area of ^{107}Ag and ^{109}Ag peaks) over all spectra × mean molar mass of Ag (107.868)]/[(accumulated signal of ^{124}Sn over all spectra × 100/5.79) × mean molar mass of Sn (118.71)].

charge effects, either at the sample surface or in the laser ablation plume. These effects occur at very high laser pulse intensity where the space charge contained in the ablated plume becomes so large that it affects the trajectories of the ions inside the plume. Hence, the ion optical system of the mass spectrometer cannot guide these ions well anymore. This results in a reduced mass resolution, which affects the quantification capabilities of our system. Therefore, the RSC value is larger than 1 for the C6 ablation experiment. Figure S3 in the SI shows mass spectra obtained at different laser pulse energies stated in Figure 3 illustrating the described effects. All depth profiling data presented in the following were acquired using the laser pulse energy as in the C4 case, i.e. 0.33 μJ.

In industrial applications, composition analysis for quality control of electrodeposited SnAg solder bumps is mostly performed by means of two well-established measurement techniques, i.e., EDX (semiquantitative) or ICP-MS (quantitative). Figure 4 shows composition analysis results obtained by these two approaches for the Ag content (wt %) found in SnAg films of 5 μm height as a function of the Ag content used in the plating bath. It is clearly observed from both data sets (EDX: black ● and ICP-MS: orange ●, respectively) that the Ag content in the alloy matrix is a linear function of the Ag content in the plating bath for the investigated SnAg films (Figures S4 and S5 in the SI demonstrate the transferability between experimental findings for SnAg films and layers). A systematic discrepancy between the values obtained by EDX and ICP-MS is apparent. This is mostly because in EDX-based determination of the Ag content in SnAg, the overlap of the Ag L with the Sn L lines significantly impairs its precise quantitation (see Figure S6 in the SI).[14] Moreover, EDX gives information only on an excited fraction (the respective volume of which depends on the used accelerating voltage of the electron beam, the working distance and the sample identity) of the probe. As can be seen in Figure S7, this concomitant with detector limitations hinders spatially highly resolved compositional analysis based on EDX

DOI: 10.1021/acs.analchem.9b04530
Anal. Chem. 2020, 92, 1355−1362

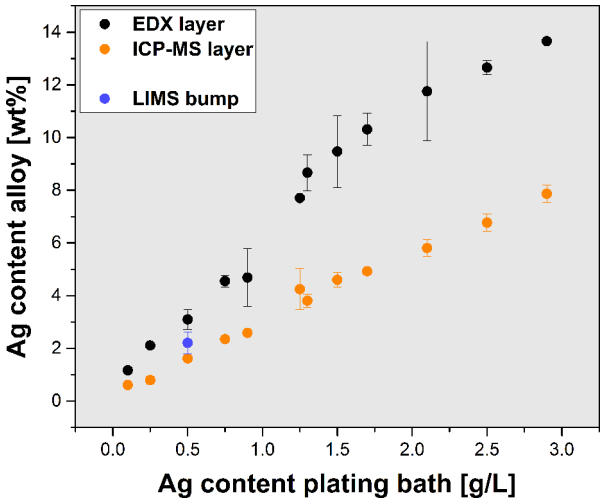

Figure 4. Comparison of the Ag alloy content in 5 μm thick SnAg solder films as a function of the Ag content in the plating bath. Platings were carried out with Chemistry A and plating parameters 1 (see Tables 1 and 2, respectively). The Ag alloy content was determined by EDX (black ●) and ICP-MS (orange ●). EDX data were averaged over 2 independent layer samples with 3 analysis spots each. ICP-MS data were averaged over two independent, entirely acidly dissolved layer samples. The purple data point represents the result obtained from averaging 5 individual LIMS experiments (see Figure S8 in the SI) on 10 μm thick SnAg bumps plated from a compositionally equal bath and with similar plating parameters as the 5 μm films (see Figures S4 and S5 in the SI for details on transferability of compositional analysis results between different layer thicknesses and different substrates).

mappings. ICP-MS yields global information on the entire, acidly dissolved sample. Due to these aspects, ICP-MS has to be considered the more accurate composition analysis approach than EDX. However, due to the required dissolution of the bump features, standard ICP-MS does not provide spatially resolved data on the element distributions within the SnAg alloy bump. Furthermore, both EDX and ICP-MS cannot be considered suitable for quantitation of the expected organic contaminants. In contrast, the LIMS-based chemical depth profiling approach is capable, as has been shown in previous studies,[9b,c,f] to provide spatially resolved composition data with nm vertical and micrometer lateral resolution both for the major metal constituents of the alloy as well as for the minor organic contaminants.

To assess the general comparability between results obtained with our LIMS-based approach and those determined with EDX and ICP-MS, respectively, the purple data point in Figure 4 shows the mean value for the Ag weight fraction as determined from 5 individual LIMS measurements of SnAg bumps deposited from a plating bath containing 0.5 g/L Ag with equivalent plating parameters as for the respective analyzed film sample. Figure S8 in the SI shows the individual five measurements. In the LIMS measurements, the entire bumps were ablated. The LIMS experiments therefore had comparable boundary conditions as the ICP-MS experiments where entirely dissolved bumps were investigated. For the comparison shown in Figure 4, the weight fraction of Ag as determined by LIMS was calculated with respect to the SnAg matrix only (i.e., without consideration of organic impurities) as was the case for the EDX and the ICP-MS data as well. The LIMS result comes to lie in between the values obtained by EDX and ICP-MS, which supports the robustness of the LIMS approach in comparison to the industrially established other two methodologies. For ICP-MS, this had already been demonstrated in a previous publication.[9e] To gain statistically more decisive and detailed insights into the comparability of results it would be desirable to analyze a larger series of both SnAg layers and bumps with all three approaches.

Figure 5 panel a shows the results for depth profiling measurements acquired at C4 laser conditions (0.33 μJ) and

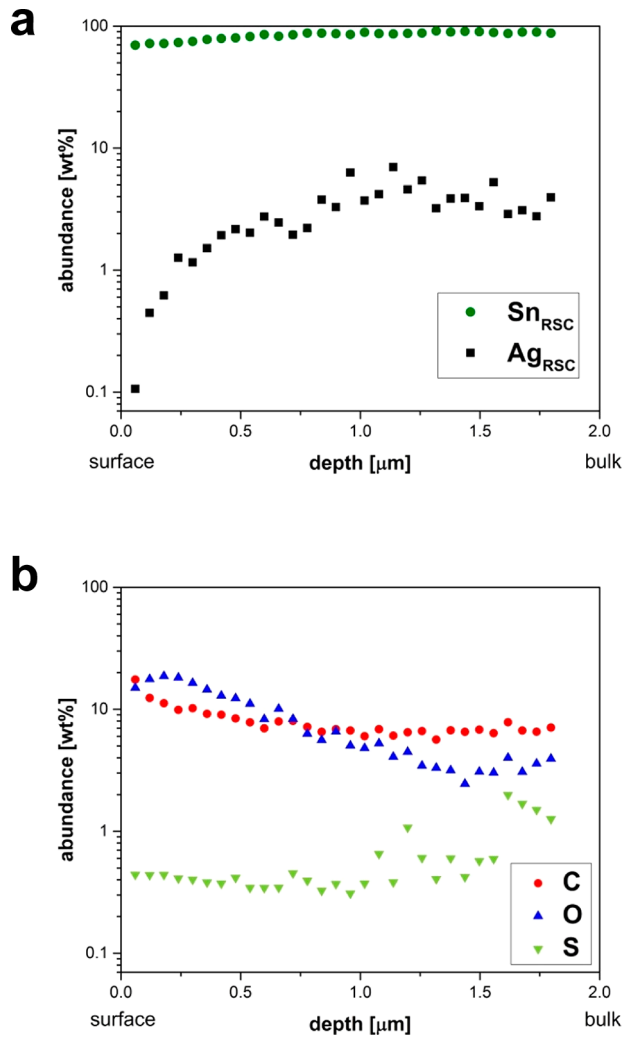

Figure 5. Depth profiling results of the surface and early bulk region of a SnAg solder bump, each data point represents a 2D layer binned over 121 single laser shots arranged on the surface of the bump. (a) Matrix-matched RSC-corrected data for Sn and Ag are shown. (b) Data for the most important organic contaminants C, O, and S. Note the clear surface effect in the beginning of the depth profile in both (a) and (b).

calibrated with the experimentally determined RSC value (0.89) over 30 2D layers with 121 crater shot positions binned each. Note, this is the first report on matrix-matched RSC-corrected LIMS depth profiling data on the chemical composition of SnAg solder alloy. The *x*-axis gives the depth of proceeding analysis (0 = bump surface) as determined by interferometric analysis of the bump height before and after the measurement. An SEM image showing the resulting morphology of the bump after this measurement can be found in Figure S9. In Figure 5, a noticeable surface effect can be observed, most strikingly for the low abundant Ag component. It manifests in the form of a

DOI: 10.1021/acs.analchem.9b04530
Anal. Chem. 2020, 92, 1355−1362

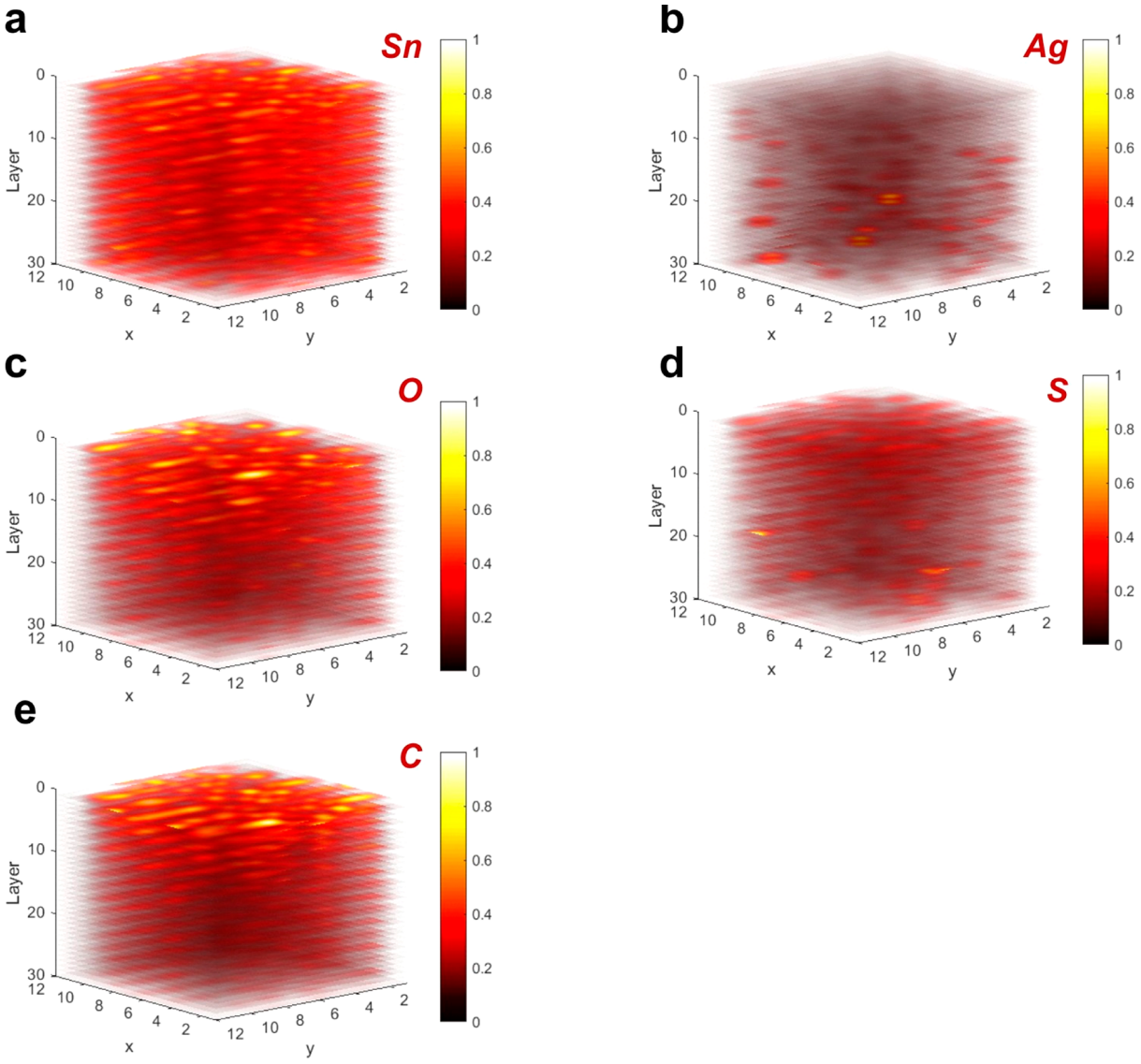

Figure 6. 3D representation of single laser shot signal intensity distribution of Sn, Ag, and the most relevant organic contaminants C, O, and S within the surface and early bulk region of the SnAg solder bump analyzed in Figure 5 by the 2D layer binning approach. Differences in the alloy homogeneity and the spatial distribution of individual organic plating bath constituents are apparent. Data have been normalized to the maximum signal intensity for this representation.

pronounced signal increase in the very beginning of the erosion process which can at least partially be attributed to the inherent surface roughness of the topmost bump region. After ablation of the first few surface layers, the signal gradually stabilizes, and a steady-state regime appears to be reached around 1 μm depth. However, also from this point on, the Ag signal fluctuates noticeably from layer to layer. This is in agreement with the nature of the SnAg alloy structure: As the solid state solubility of Ag in Sn is very low, it is commonly observed that the intermetallic Sn_3Ag ε-phase segregates from the Sn matrix when the electrodeposition is carried out from additive-free plating baths.[1b,15] With the right choice of complexing agents, this separation can be minimized. However, depending on the quality of the used additives, the Sn_3Ag intermetallic phase will still be granularly dispersed throughout the alloy matrix.

In Figure 5 panel b the other important elements of interest to our study, i.e., the major expected contaminants C, O, and S from the organic plating additives and the electrolyte, as measured for the same experiment shown in Figure 5 panel a are plotted together. Note that no noticeable change in ablation rate of the sample material is expected due to the presence of minor organic contaminations based on previous LIMS depth profiling studies using the LMS instrument.[10b] Also for the elements C and O, the previously described surface effect can be observed, with an initially high abundance of the signal followed by a decay with depth and a stabilization around the depth of 1 μm. It becomes obvious from this measurement that, as expected, not only is the inherent sample surface roughness the cause of the surface effect, but that also the elevated chemical contamination of the surface contributes importantly to this effect, which can most pronouncedly be seen in the development of the C and O signal with depth. C and O are most abundant in the outermost surface region, which can be explained by the presence of an oxide layer as well as remains of the plating bath constituents on the bump surface. These signals then show a clear decrease in concentration toward the near-surface bulk alloy region. However, a noticeable fraction of C and O is observed even at the depth of 2 μm where the composition completely stabilized.

DOI: 10.1021/acs.analchem.9b04530
Anal. Chem. 2020, 92, 1355−1362

In contrast to this, S shows almost no signal increase in the beginning of the layer ablation process and remains nearly constant from the surface up to the bulk. This indicates that there are individual, noncoupled trends in the distribution of contaminating elements within the SnAg alloy, and, most importantly, that there is a significant contribution of organic elements to the alloy matrix, at the level of percent, not only at the very surface of the alloy bump. Figure S10 shows a comparison between two depth profiling experiments at similar experimental conditions performed on two individual SnAg bumps.

Figure 6 is a 3D representation of the data presented in Figure 5 panels a and b where all measurements are displayed as unbinned single shot data points and plotted to individual pixels of the investigated 3D sample volume. The maximum signal intensity of each element was normalized to 1 in these plots. As not only the question of presence of organic contaminants in the solder bump is of urgent interest, but also their distribution and the general homogeneity of the deposited alloy are of major importance for the performance of a solder joint, this representation helps to assess whether an analyzed SnAg bump can be considered of high quality or not.

Panel a shows the Sn signal intensity throughout the investigated bump volume. As expected, Sn as the major constituent of the alloy matrix is found with homogeneous intensity distribution. In contrast to this, the distribution of Ag, as displayed in panel b, is highly heterogeneous within the three-dimensional alloy structure. Ag appears in localized clusters where its abundance is significantly increased compared to the bulk value, which can be recognized as Ag signal fluctuations in Figure 5a. The localized Ag clusters resemble the intermetallic Sn_3Ag ε-phase. Apparently, the complexing agent used in this electrodeposition experiment was not able to ensure a completely homogeneous intermixing of this intermetallic phase with the Sn matrix. We do not observe any correlation in composition between the distribution of Ag and any of the main contaminants, i.e., O, S, and C, in the 3D data, as depicted in Figure 6 panels c−e. This speaks against a systematic embedment of the complexing agent along with Ag, which is highly important information for the plating process. C and O are most abundant on the outermost surface layers of the SnAg bump, as already indicated in Figure 5 panel b. This observation can be rationalized by the residual electrolyte that remains present in a dried form on the surface of the alloy deposit after its emersion from the plating bath. In addition the near surface regime of the deposit undergoes an oxidation when exposed to the air. However, there is still a noticeable, rather homogeneous weight fraction of both O and C detectable in the early bulk region, which hints at a certain degree of embedment of both elements from separate sources, e.g., different additives or other plating bath constituents. Different origins of C and O are plausible, as there is no indication for systematic coembedment of the two elements from the distribution of their signal intensities. Different from C and O, S, which is also a major constituent of the electrolyte (see Table 1), is not accumulated to the highest extent on the very surface of the bump, but similar to Ag appears in high intensity localized clusters throughout the investigated electrodeposit volume, which are uncorrelated with the Ag clusters. Furthermore, the S concentration is significantly lower than the concentrations of O and C, which indicates that the plating bath is not embedded as an entity, but rather single components of it or single plating additives. Yet, there is no clear correlation with Ag, indicating that the source of S embedment is not the Ag complexing agent, and it is not forming silver sulfide clusters. Further studies on bumps plated from different plating bath compositions are required to conclusively assess these possible correlations, however valuable insights on the SnAg plating mechanism could be obtained from this first study.

CONCLUSIONS

This is the first report on three-dimensionally resolved, chemical composition depth profile analysis on industrially highly relevant SnAg solder bumps performed using a UV fs LIMS setup and a novel 2D binning approach for depth profiling. Elaboration of matrix-matched RSC values for Sn and Ag from a certified reference material allowed for accurate quantification of the metallic phases of the alloy. While the LIMS-based bulk quantification of the Ag content in the alloy matrix is in good agreement with results from the well-established ICP-MS technique, our approach is clearly superior with respect to spatial resolution as well as the detection and possible quantitation of organic contaminants within the investigated material. This aspect is of particular importance to obtain a deepened understanding of the additive-assisted SnAg plating process, which hitherto remains unelucidated. The analysis methodology presented herein provides important contributions to address this knowledge gap.

The LIMS-based 2D binning approach is robust enough to address the specific difficulties related to the analysis of the surface and near-surface bulk region of SnAg solder bumps. The obtained three-dimensionally resolved results on elemental distributions clearly outperform classical 1D depth profiling approaches, as these inevitably fail in accurately assessing the global composition of SnAg solder arrays given the inhomogeneous, localized appearance of several elements, especially Ag. Our experimental approach provides a reproducible and statistically decisive analysis tool to obtain a deepened global understanding of the SnAg plating process. The possibility to elucidate distinct trends in the distributions of individual elements and to assess compositional homogeneity of the alloy matrix will definitely find application for industrial screening and optimization of plating additive packages. Further optimizations of the spatial resolution of our LIMS system are planned for upcoming experiments addressing in more detail the degree of laser spot overlay in the layer shot scheme and the pulse count per single laser spot position.

ASSOCIATED CONTENT

Supporting Information

The Supporting Information is available free of charge at https://pubs.acs.org/doi/10.1021/acs.analchem.9b04530.

SEM and AFM investigations of roughness development with increasing deposit layer thickness; systematic studies on the Ag alloy content in dependence on the Ag content in the plating bath and on the identity of the wafer substrate (blanket/patterned) as analyzed by means of EDX; EDX spectrum and mappings explaining the difficulties of quantification of Ag in an SnAg alloy sample; SEM images showing the SnAg surface after the LIMS experiments; mass spectra illustrating the effect of different laser pulse energies; and data on reproducibility of LIMS measurements (PDF)

DOI: 10.1021/acs.analchem.9b04530
Anal. Chem. 2020, 92, 1355−1362

AUTHOR INFORMATION

Corresponding Author

*Phone: +41316314269. E-mail: alena.cedeno@dcb.unibe.ch.

ORCID

A. Cedeño López: 0000-0002-4917-7355
A. Riedo: 0000-0001-9007-5791
P. Moreno-García: 0000-0002-6827-787X
P. Wurz: 0000-0002-2603-1169
P. Broekmann: 0000-0002-6287-1042

Notes

The authors declare no competing financial interest.

ACKNOWLEDGMENTS

This work was supported by the Swiss National Science Foundation. We gratefully acknowledge the supply of chemicals by BASF SE, Ludwigshafen, Germany and the wafer supply by IMEC, Leuven, Belgium as well as the technical and material support by IBM Research Zurich, Switzerland. A.R. acknowledges support from the European Union's Horizon 2020 research and innovation program under the Marie Skłodowska-Curie grant agreement No. 750353.

REFERENCES

(1) (a) Lau, J. H. *J. Electron. Packag.* **2016**, *138* (3), 030802−030823. (b) Abtew, M.; Selvaduray, G. *Mater. Sci. Eng., R* **2000**, *27* (5), 95−141.

(2) (a) Han, C.; Liu, Q.; Ivey, D. G. *Mater. Sci. Eng., B* **2009**, *164* (3), 172−179. (b) Joseph, S.; Phatak, G. J. *Surf. Coat. Technol.* **2008**, *202* (13), 3023−3028. (c) Kim, J. Y.; et al. *J. Electron. Mater.* **2004**, *33* (12), 1459−1464. (d) Qin, Y.; Wilcox, G. D.; Liu, C. In *IEEE 2nd Electronics System-Integration Technology Conference*; 2008; pp 833−838. (e) Hrussanova, A.; Krastev, I. *J. Appl. Electrochem.* **2009**, *39* (7), 989−994. (f) Kim, B.; Ritzdorf, T. *J. Electrochem. Soc.* **2003**, *150* (9), C577−C584. (g) Qin, Y.; Wilcox, G.; Liu, C. *Electrochim. Acta* **2010**, *56* (1), 183−192.

(3) Kiumi, R.; et al. In *IEEE Electronic Components and Technology Conference*, 2005; pp 120−126.

(4) (a) Margetic, V.; Bolshov, M.; Stockhaus, A.; Niemax, K.; Hergenröder, R. *J. Anal. At. Spectrom.* **2001**, *16* (6), 616−621. (b) Vadillo, J. M.; Palanco, S.; Romero, M.; Laserna, J. *Anal. Bioanal. Chem.* **1996**, *355* (7−8), 909−912.

(5) Pisonero, J.; Koch, J.; Wälle, M.; Hartung, W.; Spencer, N.; Günther, D. *Anal. Chem.* **2007**, *79* (6), 2325−2333.

(6) (a) Mateo, M. P.; Garcia, C. C.; Hergenröder, R. *Anal. Chem.* **2007**, *79* (13), 4908−4914. (b) Pisonero, J.; Günther, D. *Mass Spectrom. Rev.* **2008**, *27* (6), 609−623.

(7) Koch, J.; Günther, D. *Appl. Spectrosc.* **2011**, *65* (5), 155−162.

(8) (a) Houk, R. S. *Anal. Chem.* **1986**, *58* (1), 97A−105A. (b) Luong, E. T.; Houk, R. S. *J. Am. Soc. Mass Spectrom.* **2003**, *14* (4), 295−301.

(9) (a) Moreno-Garcia, P.; Grimaudo, V.; Riedo, A.; Cedeno Lopez, A.; Wiesendanger, R.; Tulej, M.; Gruber, C.; Lortscher, E.; Wurz, P.; Broekmann, P. *Anal. Chem.* **2018**, *90* (11), 6666−6674. (b) Cedeño López, A.; Grimaudo, V.; Moreno-García, P.; Riedo, A.; Tulej, M.; Wiesendanger, R.; Wurz, P.; Broekmann, P. *J. Anal. At. Spectrom.* **2018**, *33* (2), 283−293. (c) Grimaudo, V.; Moreno-García, P.; Cedeño López, A.; Riedo, A.; Wiesendanger, R.; Tulej, M.; Gruber, C.; Lörtscher, E.; Wurz, P.; Broekmann, P. *Anal. Chem.* **2018**, *90* (8), 5179−5186. (d) Grimaudo, V.; Moreno-García, P.; López, A. C.; Riedo, A.; Wiesendanger, R.; Tulej, M.; Gruber, C.; Lörtscher, E.; Wurz, P.; Broekmann, P. *Anal. Chem.* **2018**, *90* (4), 2692−2700. (e) Grimaudo, V.; Moreno-García, P.; Riedo, A.; Meyer, S.; Tulej, M.; Neuland, M. B.; Mohos, M.; Gütz, C.; Waldvogel, S. R.; Wurz, P.; Broekmann, P. *Anal. Chem.* **2017**, *89* (3), 1632−1641. (f) Riedo, A.; Grimaudo, V.; Cedeño López, A.; Tulej, M.; Wurz, P.; Broekmann, P. *J. Anal. At. Spectrom.* **2019**, *34* (8), 1564−1570.

(10) (a) Riedo, A.; Neuland, M.; Meyer, S.; Tulej, M.; Wurz, P. *J. Anal. At. Spectrom.* **2013**, *28* (8), 1256−1269. (b) Grimaudo, V.; Moreno-García, P.; Riedo, A.; Neuland, M. B.; Tulej, M.; Broekmann, P.; Wurz, P. *Anal. Chem.* **2015**, *87* (4), 2037−2041. (c) Riedo, A.; Bieler, A.; Neuland, M.; Tulej, M.; Wurz, P. *J. Mass Spectrom.* **2013**, *48* (1), 1−15.

(11) Wiesendanger, R.; Wacey, D.; Tulej, M.; Neubeck, A.; Ivarsson, M.; Grimaudo, V.; Moreno-García, P.; Cedeño-López, A.; Riedo, A.; Wurz, P. *Astrobiology* **2018**, *18* (8), 1071−1080.

(12) Woertink, J.; Qin, Y.; Prange, J.; Lopez-Montesinos, P.; Lee, I.; Lee, Y.; Imanari, M.; Dong, J.; Calvert, J. In From C4 to micro-bump: Adapting lead free solder electroplating processes to next-gen advanced packaging applications, 2014. *IEEE 64th Electronic Components and Technology Conference (ECTC), 27−30 May 2014*; 2014; pp 342−347.

(13) Neuland, M. B.; Grimaudo, V.; Mezger, K.; Moreno-García, P.; Riedo, A.; Tulej, M.; Wurz, P. *Meas. Sci. Technol.* **2016**, *27* (3), 035904.

(14) Eckert, R. *Scanning* **1986**, *8* (5), 232−238.

(15) McCormack, M.; Jin, S.; Kammlott, G. W.; Chen, H. S. *Appl. Phys. Lett.* **1993**, *63* (1), 15−17.

(16) Lau, J. H. Recent Advances and New Trends in Flip Chip Technology. *J. Electron. Packag.* **2016**, *138* (3), 030802.

DOI: 10.1021/acs.analchem.9b04530
Anal. Chem. 2020, 92, 1355−1362